



Water Resources Research®

RESEARCH ARTICLE

10.1029/2025WR039992

Special Collection:

Advances in large-scale hydrological modeling and prediction under global change

Key Points:

- A two-month lifespan of a 3D flood structure, encompassing flood extent and depth across the 229,000 km² Hai River Basin, was reconstructed
- Flood detention areas activated during the 2023 flood detained 2.7 billion m³ of floodwaters, with the majority drained within two weeks
- River conveyance capacity was a critical determinant during the drainage process of flood detention areas

Supporting Information:

Supporting Information may be found in the online version of this article.

Correspondence to:

X. Hu,
hu.xie@pku.edu.cn

Citation:

Lin, Y., Hu, X., Wang, F., Tang, Q., Zhao, Y., Li, Y., et al. (2025). Quantifying the lifespan of 3D flood structures: Unlocking the potential of flood detention areas for enhanced flood control in China. *Water Resources Research*, 61, e2025WR039992. <https://doi.org/10.1029/2025WR039992>

Received 17 JAN 2025

Accepted 21 OCT 2025

Author Contributions:

Conceptualization: Xie Hu

Data curation: Xie Hu, Yong Zhao, Yongsheng Li, Tao Li, Changjun Liu

Funding acquisition: Xie Hu

Methodology: Yiling Lin, Xie Hu

Resources: Fang Wang, QiuHong Tang, Xiekang Wang, Dongfeng Li

Supervision: Xie Hu

Visualization: Yiling Lin

Quantifying the Lifespan of 3D Flood Structures: Unlocking the Potential of Flood Detention Areas for Enhanced Flood Control in China

Yiling Lin¹ , Xie Hu¹ , Fang Wang², QiuHong Tang³ , Yong Zhao⁴ , Yongsheng Li⁵, Tao Li⁶, Changjun Liu⁷, Xiekang Wang⁸, and Dongfeng Li⁹

¹College of Urban and Environmental Sciences, Peking University, Beijing, China, ²River Basin Habitats Research Center, College of Architecture and Landscape Architecture, Peking University, Beijing, China, ³Key Laboratory of Water Cycle and Related Land Surface Processes, Institute of Geographic Sciences and Natural Resources Research, Chinese Academy of Sciences, Beijing, China, ⁴Department of Water Resources, China Institute of Water Resources and Hydropower Research, Beijing, China, ⁵National Institute of Natural Hazards, Ministry of Emergency Management of China, Beijing, China, ⁶Land Satellite Remote Sensing Application Center, Ministry of Natural Resources of China, Beijing, China, ⁷Hai River Water Conservancy Commission, Ministry of Water Resources of China, Beijing, China, ⁸State Key Laboratory of Hydraulics and Mountain River Engineering, Sichuan University, Chengdu, China, ⁹Key Laboratory for Water and Sediment Sciences, Ministry of Education, College of Environmental Sciences and Engineering, Peking University, Beijing, China

Abstract The escalating frequency and magnitude of floods pose significant challenges to traditional flood control measures with fixed defense capacities, such as levees, dams, and reservoirs. Flood Detention Areas (FDAs) have been widely implemented in many countries as solutions to extreme flood events, functioning by temporarily holding excess floodwaters and serving as farmland and residential zones during periods of inactivity. However, uncertainties regarding their flood control effectiveness, concerns over post-activation livelihood recovery, and the lack of management guidelines have limited their broader adoption and effective utilization. Here we proposed an innovative remote sensing and AI based framework to derive the lifespan of 3D flood structure incorporating flood extent and depth. Taking the once-in-a-century flood in China's Hai River Basin (HRB) in 2023 as example, the thrived two-month-long catchment-scale 229,000-km² 3D flood structure enabled the first quantitative evaluation to the flood control and drainage capacities of FDAs. The results revealed that eight activated FDAs detained 2.7 billion m³ of floodwaters, with most of the water drained within two weeks. River conveyance capacity was identified as a pivotal factor in the flood drainage process. The 3D flood structure further highlights disparities in detention processes between upstream and downstream FDAs due to cascade effects, providing valuable guidance for their management. These findings resolve the key uncertainties and debates regarding FDAs, providing insights to enhance FDA management, and supporting their broader implementation in flood-prone regions with extensive agricultural land use and dense populations, thereby mitigating future flood risks and minimizing associated losses.

Plain Language Summary The unprecedented floods with increasing frequency demand sustainable solutions. Flood Detention Areas (FDAs) therefore emerged and have been widely implemented to temporarily detain excessive floodwaters. Using the 3D flood structure of a once-in-a-century flood in China's Hai River Basin (HRB) in 2023, we provided the first quantitative assessment to the activated FDAs, which detained 2.7 billion m³ of floodwaters and drained them within two weeks. Further analysis proved the critical role of river conveyance capacity during flood drainage and revealed disparities between upstream and downstream FDAs. These findings deepen understanding to FDAs, offering insights to enhance management, and supporting their broader adoption in flood-prone regions, further mitigating the future flood risks and losses.

1. Introduction

Levees, dams, and channelization have been used to safeguard lives and properties from devastating floods since the dawn of civilization (Grill et al., 2019). However, Extreme flood events have become more frequent in recent decades due to global climate change (Merz et al., 2021), and the designed measures are not always effective in managing devastating floods, resulting in significant losses (Kreibich et al., 2022; Munoz et al., 2018). Additionally, the implementation of these measures may lead to side effects, such as increasing peak flows (Ansari

Writing – original draft: Yiling Lin
Writing – review & editing: Yiling Lin, Xie Hu, Fang Wang, QiuHong Tang, Yong Zhao, Yongsheng Li, Tao Li, Changjun Liu, Xiekang Wang, Dongfeng Li

et al., 2024), jeopardizing ecosystem services and biodiversity (Galelli et al., 2022; Winemiller et al., 2016), and enlarging socioeconomic disparities (Kind et al., 2016). Therefore, in response to intensified heavy precipitation associated with global climate change, the contemporary concept of “Room for the River” has been prioritized over the continuous elevation of defense levels to reduce peak flows (Alfieri et al., 2016; Opperman et al., 2009). The implementation of the Flood Detention Areas (FDAs) (Arrighi et al., 2018; Chan et al., 2019), drainage systems (Barbour et al., 2022), afforestation (Buechel et al., 2022), and river renaturation (Grafton et al., 2015) are viable approaches for peak flow reduction.

Among these measures, FDAs reduce peak flows by temporarily detaining floodwaters when the flow exceed the capacities of levees, dams, reservoirs, and other infrastructures, thereby relieving flood pressure on downstream regions. Following the failure of levees and dams in unprecedented flood events, the FDAs have become a key component of flood management systems in many countries including China (DRC, 2022), the United States (Pearcy, 1996), Germany (State Ministry of the Environment Baden-Württemberg, 2007), the United Kingdom (Van Doorn-Hoekveld & Groothuijse, 2014), and the Netherlands (Van Doorn-Hoekveld & Groothuijse, 2017). Especially, in China, FDAs are extensively implemented, with 98 located across major rivers such as the Yangtze and Hai (DRC, 2022). And these FDAs have been instrumental in mitigating the impacts of unprecedented flood events (Dottori et al., 2023; Nittrouer et al., 2012). From 1950 to 2021, China activated 66 FDAs for 424 times, with a cumulative flood detention volume of 140 billion m³ (DRC, 2022). Additional to the flood control, FDAs serve various purposes, such as agriculture, forestry, and fishing, when they are not activated (Morton & Olson, 2013; State Ministry of the Environment Baden-Württemberg, 2007). In China, due to big population and urban sprawl, 16.56 million people now reside in 98 FDAs that also host approximately 1.73 million hectares of farmland (DRC, 2022).

Despite the widespread implementation of FDAs, their multifunctional nature continues to provoke debates and uncertainties (Barker, 2013; Serra-Llobet et al., 2021). The activation of FDAs can result in losses, such as the flooding of farmlands and built-up areas within FDAs. Therefore, it is crucial to demonstrate that the significant advantages of FDAs to the broader watershed outweigh these losses to justify their activation. However, the absence of quantitative assessments of FDAs' flood control benefits impedes their justification, fostering skepticism about their necessity. Meanwhile, concerns over whether the communities within FDAs can recover from the post-activation flooding also raises inquiries. A key factor influencing recovery is the drainage duration of detained floodwater, which can affect crop yields, post-flood reconstruction, as well as the restoration of daily life and production activities (Han et al., 2024). However, the drainage duration remains indeterminate. In addition to these debates, the absence of reliable guidelines for the management and activation of FDAs poses significant risks. Previous cases have demonstrated that delayed activation and improper management can result in flood control failures and even intensify the impacts of disasters (Olson & Morton, 2013). These uncertainties and debates restrict the wider integration of FDAs into flood management systems and impede the timely activation and effective management of existing FDAs during flood events, ultimately diminishing their capacity to better control flooding.

Bearing these unsolved controversies and debates, we selected Hai River Basin (HRB) hosting 28 FDAs as a representative study area. The flood frequency and magnitude of extreme floods in HRB are severe and continue to increase, with 29 catchment-scale extreme floods over the past half a millennium, 7 occurring in the past century, and 4 in the 21st century alone (Hai River Chronicles Compilation Committee, 1997). This situation necessitates an increased capacity for flood detention in FDAs. On the other side, the HRB, encompassing the Beijing-Tianjin-Hebei metropolis, is home to 160 million population and remains a pivotal agricultural production hub in China. Moreover, in HRB, the winter wheat is sown from late September to late October and harvested in early to middle-June, and the summer maize is usually planted immediately after the wheat harvest and matures in late September (Liang et al., 2011). The flood season in HRB typically falls between late July and early August. Extended waterlogging adversely affects summer maize and poses a risk to the planting of winter wheat, as well as the subsequent year's harvest. Therefore, HRB demands rapid flood drainage after activation of FDAs.

In 2023, Typhoon Dokuri brought an estimated 49 million cubic meters of precipitation from 28 July to 2 August over the western windward slopes of HRB (Figure 1a). The massive rainfall surged into the river channels and was swiftly transported from the western mountainous areas to the central and eastern plains, triggering a once-in-a-century catastrophic flood. To mitigate the flood, eight FDAs were sequentially activated from 30 July to 2

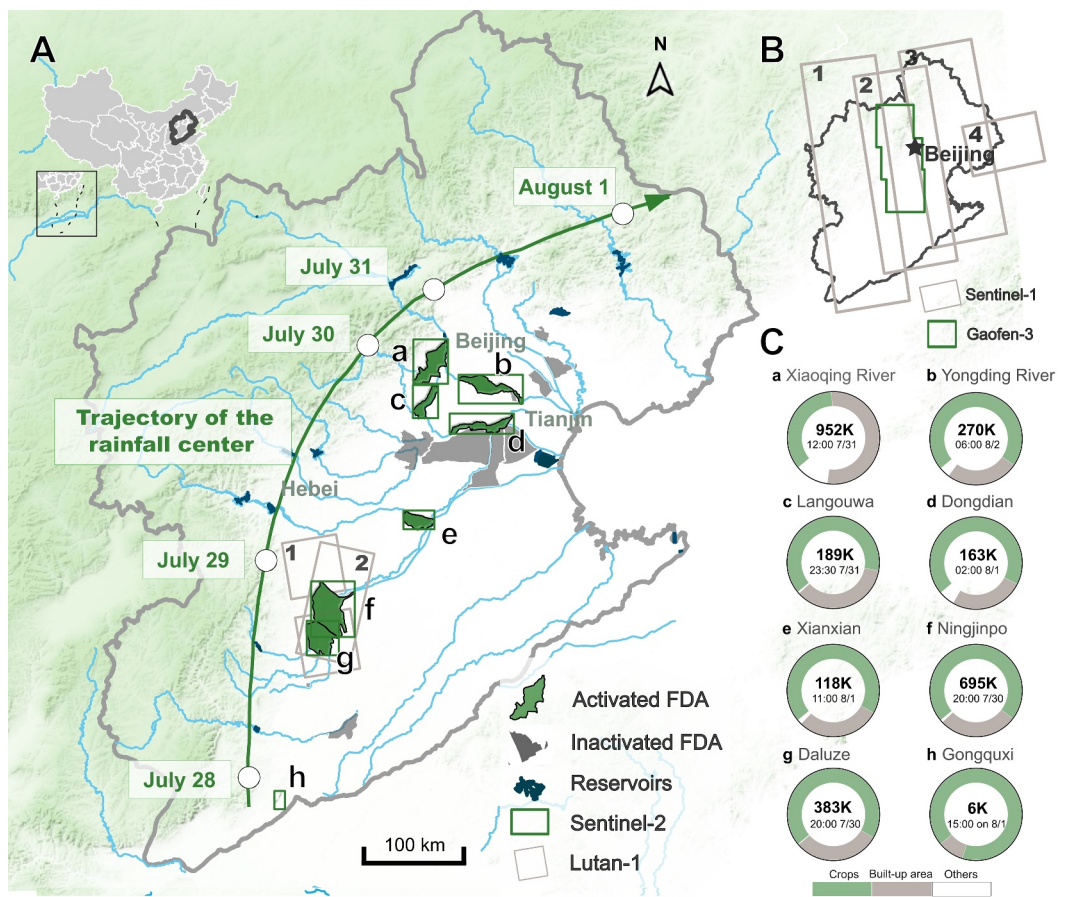


Figure 1. Study area and data. (a) Geographic locations of activated and inactivated FDAs, along with the trajectory of the rainfall center. Footprints of Sentinel-2 and Lutan-1 remote sensing images were indicated with boxes. The number above the footprint of Lutan-1 represented its orbit ID in Table S2 in Supporting Information S1. (b) Footprints of Sentinel-1 and Gaofen-3 remote sensing images. The number above the footprint of Sentinel-1 represented its orbit ID in Table S2 in Supporting Information S1. (c) Land use, population, and activated time of activated FDAs. The bold words within the pie charts represent the population, while the text below indicates the activation time.

August. The enormous rainwater posed a significant challenge to the flood control capacity of activated FDAs. These FDAs are predominantly composed of farmland and built-up areas, home to 2.77 million people and contributing a GDP of 125.9 billion Chinese Yuan, thereby placing high demands on flood drainage speed to facilitate post-disaster recovery (Figure 1c). Although the engineering capacities of these FDAs (e.g., designed area and storage volume) have been provided (Table S1 in Supporting Information S1), their actual flood detention and drainage capacities during real, devastating floods have not yet been quantitatively assessed. Taking the unprecedented flood in HRB, 2023 as example, here we aimed to answer the following questions: (a) Did the 8 activated FDAs provide significant benefits to managing the catastrophic flood, and how much floodwater was detained by these FDAs? (b) How quickly can the detained floodwaters be drained, and is this speed sufficient for the timely recovery of agriculture and community life? (c) Is it possible for results derived from remote sensing data to serve as dependable guidelines for the management and activation of FDAs?

To solve these problems, we started from tracking floodwater footprints over the two-month flood period across the entire HRB by synergizing multi-source remote sensing images from European and Chinese satellites and deep learning framework. Next, we enhanced the Floodwater Depth Estimation Tool (FwDET) to accommodate coarse-resolution topography data, enabling inference of flood depth through the incorporation of DEM and floodwater footprints. The constructed lifespan of the 3D flood structure, incorporating the two-month flood extent and depth, can illustrate the flood control dynamics across the entire watershed and quantify the flood detention volume of FDAs, both serving as indicators of the flood control benefits provided by FDAs. Finally, the

lifespan of flood extent enables the calculation of floodwater drainage duration for each pixel within FDAs. Using the pixel-level drainage maps of the FDAs, we constructed a discrete Cumulative Distribution Function (CDF), which was then fitted with a logistic function to transform it into a continuous form, allowing us to estimate the pixel-level flood drainage duration for each FDA.

2. Data and Methods

Current methodologies are insufficient to address these uncertainties and controversies in the implementation of FDAs. Although in situ observations indicate that FDAs can reduce downstream floodwater levels, these findings are limited to localized effects and fail to capture broader impacts of FDAs across entire watersheds (Nittrouer et al., 2012). Hydrodynamics models enable simulations of dynamic 3D flood structure integrating flood extent and depth. The flood extent within a large watershed enables assessment to the overall effectiveness of flood control measures containing FDAs. Furthermore, the integration of flood extent and depth allows for the quantitative estimation of the flood detention volume and drainage duration of FDAs. However, developing these models necessitates extensive geological and hydrological data, which is time-consuming and often unavailable in many areas. And simulating unprecedent floods across large watershed require dramatic computation resources (Xu et al., 2024). Additionally, extensive simplifications and assumptions in modeling simulations create discrepancies with real flood scenarios, thereby reducing their reliability (Dottori et al., 2023; Vorogushyn et al., 2013; Wang et al., 2021).

Compared to hydrodynamics models, advanced remote sensing technique showcase promising potential for reconstructing flood extent and depth with lower data requirements and higher computational efficiency. Satellites operating within the visible and microwave regions have demonstrated exceptional capability in monitoring earth surface on a large spatial extent. The emitted electromagnetic (EM) waves from Synthesize Aperture Radar (SAR) satellites are reflected away at the interface of water surfaces, resulting in extremely weak back-scattering signals in SAR amplitude. Moreover, electromagnetic waves can penetrate clouds and rain during flood events, enabling observations even under inclement weather conditions when optical satellite visibility is obstructed by cloud cover. Therefore, SAR images have been extensively employed for flood extent delineation by combining with various algorithms such as the Otsu threshold method, machine learning, and deep learning models (Andrew et al., 2023; Grimaldi et al., 2019; Zhang et al., 2025). Additionally, algorithms for flood depth reconstruction relied solely on flood extent and topographic data have been developed (Cohen et al., 2017).

Several challenges continue to impede the effective utilization of remote sensing data in recovering reliable lifespan of 3D flood structure. Primarily, due to the extended revisit intervals of SAR sensors, capturing dynamic flood extents across extensive geographical areas requires the integration of SAR images from diverse sensors, regions, and timeframes. These SAR images possess differing polarizations and exhibit noticeable variations in color tones. Therefore, when directly applying the trained model to multi-temporal and multi-sensor SAR images, the model performance diminished significantly (Jiang et al., 2021; Lin et al., 2024, 2025). Furthermore, the prolonged revisit intervals typically lead to the omission of rapid flood peaks, resulting in the significant underestimation of floodwater detention volume of FDAs. A further challenge lies in the reconstruction of flood depth at high resolution. Current methodologies necessitate high-resolution topographic data, which is often not accessible for most of FDAs. The discrepancy between the coarser topographic data and more detailed flood extent lead to the failure of the algorithms (Cohen et al., 2017). Moreover, accurately estimating the duration of flood drainage from the temporally discontinuous remote-sensing-based 3D flood structure presents a significant issue.

2.1. Multi-Source Remote Sensing Data

Multi-source remote sensing data, including Synthetic Aperture Radar (SAR) images from Sentinel-1, Gaofen-3, and Lutan-1 satellites and optical images from Sentinel-2 satellite, were used to recover the dynamic floodwater footprints. Pre-flood Sentinel-1 Radiometric Terrain Correction (RTC) images from the Alaska Satellite Facility (ASF) were used to extract regular water bodies. Post-flood Sentinel-1 RTC images, covering the HRB, were collected between late July and late September 2023, capturing the full two-month flood footprints across the basin. To obtain floodwater footprints time series with shorter intervals, we supplemented our preliminary results from Sentinel-1 with Gaofen-3 satellite images collected on August 1st and Lutan-1 satellite images collected on August 4th and 7th. To further address the inevitable missing of floodwater margins during peak hours, caused by

the multi-day revisit intervals of SAR images, Sentinel-2 optical images collected in August and September with cloud covers less than 20% were used to map flood peaks of FDAs omitted by SAR images (Figures 1a and 1b, Tables S2 and S3 in Supporting Information S1). The Lutan-1 images were resampled to a 10-m resolution to align with the resolution of the other images.

2.2. Dynamic Flood Extent Extraction

We proposed an automated deep learning framework to extract multi-temporal flood extents across 229,000-km² HRB using SAR images in different polarizations from Sentinel-1 and Gaofen-3 satellites. To enhance semantic information in the deep learning model, dual-polarization Sentinel-1 and Gaofen-1 SAR images were combined to create false-color RGB images (Tiampo et al., 2022). We subsequently conducted histogram matching to standardize the color tones of the composite images, thereby improving the model's performance across vast areas and multi-sensors (Yun et al., 2015). We applied the DeepLabv3+ model for flood extent segmentation (Chen et al., 2018). By excluding the pre-flood water bodies, we obtained multi-temporal flood extents. Unlike Sentinel-1 and Gaofen-3 satellites in dual polarization, Lutan-1 SAR images are in the single polarization, and thus not applicable for false-color composition and deep learning approach. Instead, we applied the Otsu threshold method to extract the flood extent from Lutan-1 SAR images (Otsu, 1979). The results can be integrated with the multi-temporal flood extents thrived from Gaofen-3 and Sentinel-1 to generate flood footprint time series with shorter intervals (Figure 2a).

2.3. Flood Peak Identification

Here we introduced a new method to compensate for the unavoidable omission of flood peaks in SAR acquisitions by incorporating optical images. The flood-affected surfaces remain damp for a certain period after the flood-waters recede, whereas the areas affected only by rainfall without flooding tend to dry out more quickly. Thus, a period after the flood peaks, regions still exhibiting elevated soil moisture can be identified as the flood peak extent. The elevated soil moisture can be characterized by a higher Normalized Difference Water Index (NDWI) (Al-Ali et al., 2024). Therefore, even if the first cloud-free Sentinel-2 images are only accessible approximately one week after the flood peaks, the NDWI derived from these images can still be used to infer the maximum flood extent. Based on the principle, we selected the earliest available cloud-free Sentinel-2 images and then calculated the NDWI differences relative to the pre-flood images. By applying a threshold method, areas with elevated NDWI values were extracted and identified as the flood peak extent. Notably, areas exhibiting elevated NDWI values corresponded closely with the flood-affected regions identified in the optical images, thereby reinforcing the reliability of the method (Figure S1 in Supporting Information S1). Additionally, using multi-temporal flood extents inferred from SAR images, we can determine the earliest time point at which the flood began to recede. Thus, the timing of the flood peak was estimated as the midpoint between this time point and the preceding one (Figure 2b).

2.4. Flood Depth Solution

We improved latest version of the Floodwater Depth Estimation Tool (FwDET v2.1) (Cohen et al., 2022) to estimate flood depths based on the flood extents and the Digital Elevation Model (DEM). The floodwater depth of the flooded pixels can be estimated by the difference between the land surface elevation and the local floodwater elevation. The FwDET (v2.1) model estimates the local floodwater elevation under the assumption that variations in floodwater elevation across the cross-section are negligible. Based on this assumption, the floodwater elevation within the flood extent is assigned the topography elevation of the nearest pixel outlined the flood extent. This approach demonstrates high accuracy with a high-resolution DEM. However, spatial mismatch between the available coarse DEM and flood extent can introduce enormous artifacts (Cohen et al., 2022). To address this issue, we compared four commonly used DEMs (i.e., the Copernicus DEM GLO-30 corrected by ASF, the Copernicus DEM GLO-30, FABDEM, and SRTM DEM), and found that the ASF-corrected Copernicus DEM GLO-30 exhibited the highest consistency with both the actual elevation conditions and extracted flood extent. The high alignment originated from the resampling process, in which the 30-m resolution Copernicus DEM GLO-30 was resampled to 10-m resolution and geoid-corrected during Sentinel-1 RTC processing (Figure S2 in Supporting Information S1).

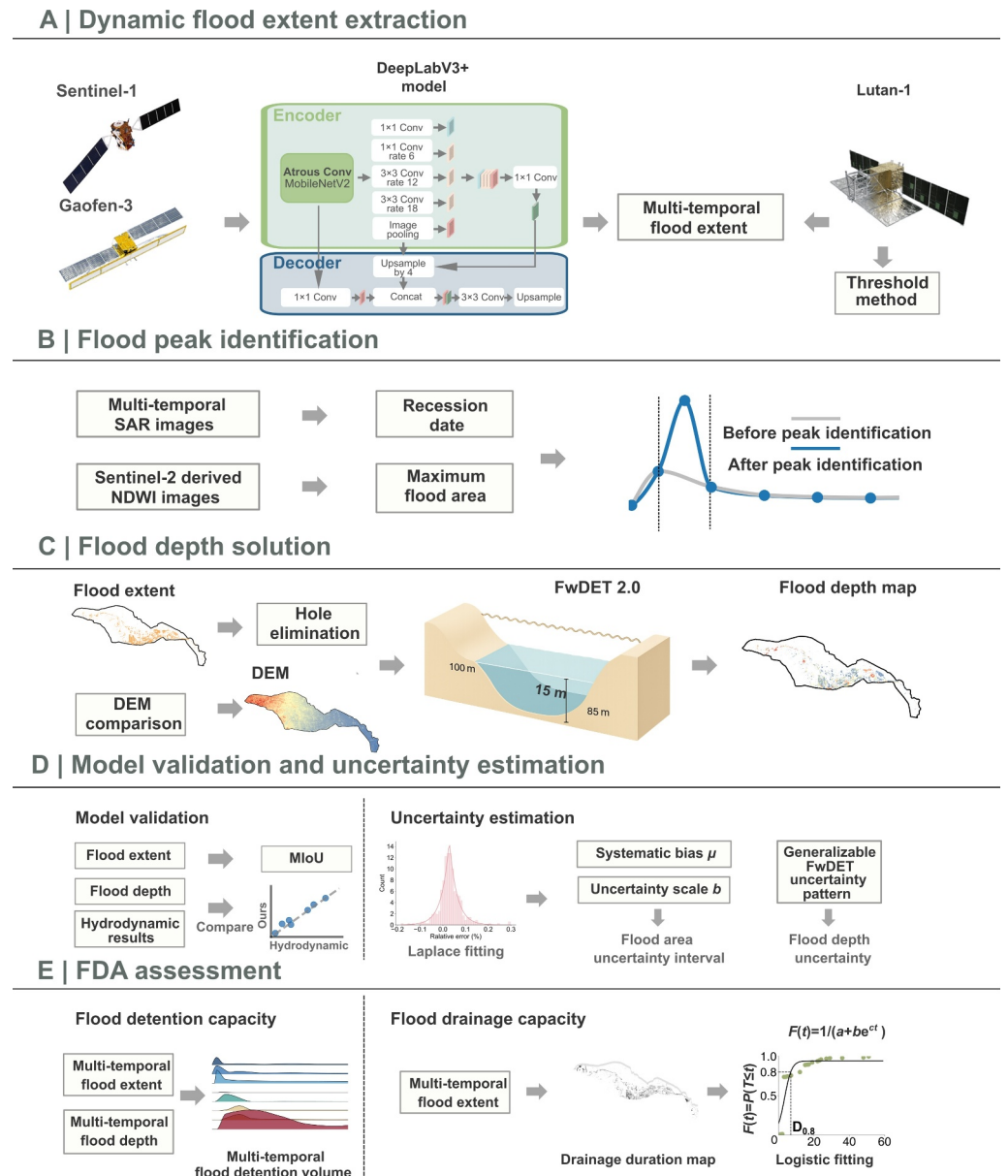


Figure 2. Flowchart of 3D flood structure lifespan recovery and FDA assessment.

However, the selected DEM with coarse resolution still lacks the finer details such as internal holes and polygons in the flood extent derived from 10-m resolution images, leading to abrupt changes or negative values in the estimated floodwater depth (Figures S3A and S3B in Supporting Information S1). To mitigate this issue, the model was further refined by filling these small internal holes and eliminating minor polygons from the flood extent data, thereby obtaining a continuous flood depth map (Figures S3C and S3D in Supporting Information S1, and Figure 2c).

2.5. Model Validation and Uncertainty Estimation

To validate the reliability of derived 3D flood structure, we first assessed the accuracy and generalizability of the flood extent extraction method across different locations, dates, and satellite sensors. Specifically, flood extents from Beijing on July 12 and Fangshan on August 1 were used for validation. The extracted flood extents were compared with manually interpreted flood extents, and the Mean Intersection over Union (MIoU) was calculated to quantify the discrepancy. For flood depth, the conventional validation approach was to compare the results with

in situ observations or with flood depths derived from hydrodynamic simulations (Teng et al., 2022). However, both in situ observations and the data required to drive hydrodynamic models (e.g., high-resolution DEM) were unavailable. Therefore, we adopted an indirect validation strategy, comparing our estimated maximum flood detention volumes with those derived from the hydrodynamic results reported by Du et al. (2023).

Besides model validation, uncertainty estimation was performed to identify systematic biases and provide confidence intervals, supporting the decision-making based on the 3D flood structure. To obtain sufficient samples for characterizing the error distribution of prediction flood area, we divided the images with ground truth (i.e., Beijing and Fangshan) into 300×300 -pixel blocks with 30% overlap. The errors of these block samples were then fitted with a Laplace distribution to derive the systematic bias μ and the uncertainty scale b , where positive μ indicates overestimation to the flood area, and negative μ indicates underestimation, and larger b corresponds to greater uncertainty. Based on these fitted parameters, the 95% confidence interval for the flood area can be expressed as:

$$A \in \left[\hat{A}(1 - \mu - 3.689b), \hat{A}(1 - \mu + 3.689b) \right] \quad (1)$$

where \hat{A} represented the prediction flood area. Furthermore, to examine how the model's uncertainty and bias varied with flood extent, we applied different thresholds of flood area ratio (the ratio of the true flooded area to the total block area). For each threshold, only blocks exceeding the threshold were included in the error samples, which were then fitted separately (See Text S1 in Supporting Information S1 for details).

For flood depth, Teng et al. (2022) demonstrated that FwDET exhibited a similar uncertainty distribution across 26 flood scenes and proved that the pattern is generalizable across a wide range of flood scenarios. Therefore, the pattern can serve as a useful reference in our flood depth uncertainty estimation (Figure 2d).

2.6. Floodwater Drainage Duration Assessment

Based on the lifespan of the flood extent, we developed a methodology to assess the drainage duration for each FDA at pixel-level. First, we recovered pixel-level drainage duration maps of FDAs. The duration of flood drainage for a specific pixel is estimated by measuring the time span from the initial observation of flooding to the earliest observation indicating that the pixel has drained. Using the pixel-level drainage duration map, we then constructed a Cumulative Distribution Function (CDF) $F(t)$ which is defined as follows:

$$F(t) = P(T \leq t) \quad (2)$$

The CDF denotes the proportion of pixels with a drainage duration T less than or equal to t , representing the percentage of pixels that can be drained within t days. We then transformed the discrete CDF $F(t)$ into a continuous form by fitting it with a logistic function, as articulated in (2):

$$F(t) = 1/(a + be^{ct}) \quad (3)$$

where the a , b , and c are fitting parameters. The pixel-level drainage duration of the FDAs was ultimately defined as the duration required for 80% of the flood pixels to be drained, expressed using the metric $D_{0.8}$. The $D_{0.8}$ can be calculated as the value of t when $F(t)$ equals 80% (Figure 2e).

3. Results

3.1. The Flood Control Across HRB

Our catchment-scale flood extent analysis demonstrated that the total flood area was only about $2,200 \text{ km}^2$, with most floodwaters trapped within the counties housing the FDAs, leaving other major cities such as Beijing and Tianjin largely unaffected. Even within these flooded areas, most floodwaters were not catastrophic but were managed as part of a planned flood control strategy. Except for Pingshan and Anxin, counties with a maximum flood extent exceeding 25 km^2 overlap with the FDAs. The residents had been evacuated in advance before FDA activation. Similarly, in Pingshan and Anxin, the flooding occurred due to the presence of the Gangnan Reservoir

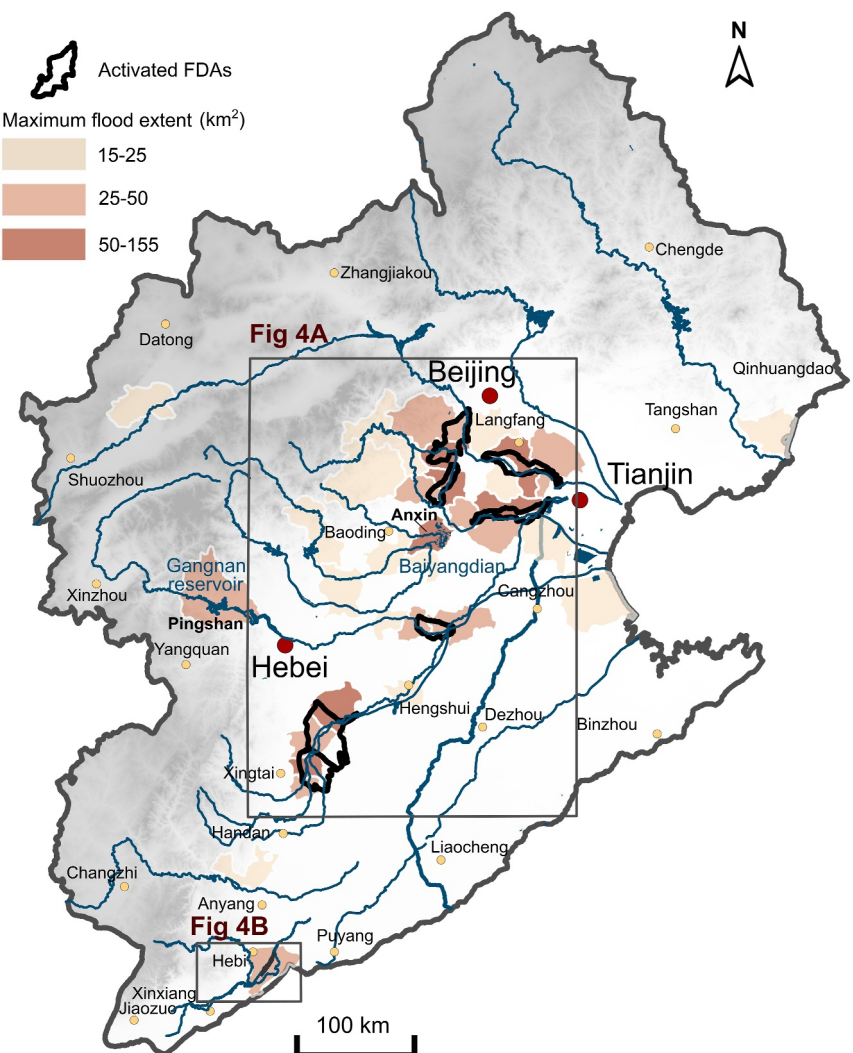


Figure 3. The counties with maximum flood extent exceeding 15 km^2 , and the black boxes outline the spatial extents of panels Figures 4a and 4b.

and the natural wetland Baiyangdian, both of which have no residents or built infrastructure (Figure 3). The catastrophic floods of 1939 (30 million m^3) and 1963 (60 million m^3), which experienced rainfall levels comparable to those in 2023 (49 million m^3), flooded approximately 66,000 km^2 and 54,000 km^2 of the HRB, accounting for 20.75% and 17.00% of the basin's total area. In contrast, only about 0.69% of the HRB was flooded in 2023, representing a significant reduction of 96.64% and 95.89% compared to the flooded extents of 1939 and 1963, respectively. The flood control measures in the HRB effectively kept floodwaters below the safety limits, thereby averting overflows and the widespread flooding and catastrophic losses seen in previous events with comparable rainfall. By both the engineering criterion of maintaining water levels within design limits and the loss-minimization criterion of reducing flood-related damages, the flood control measures in HRB can be considered successful.

The substantial reduction in flood impacts, relative to 1939 and 1963, can be ascribed to a comprehensive flood control system comprising FDAs, reservoirs, and levees established post-1963. In the upstream regions of the HRB, over 1,700 reservoirs significantly reduced the peak flows. Meanwhile, about 9,000 km of levees and over 50 manmade dredged channels regulated floodwaters in the midstream and downstream areas. FDAs were activated and alleviated floodwater pressure by detaining substantial floodwaters.

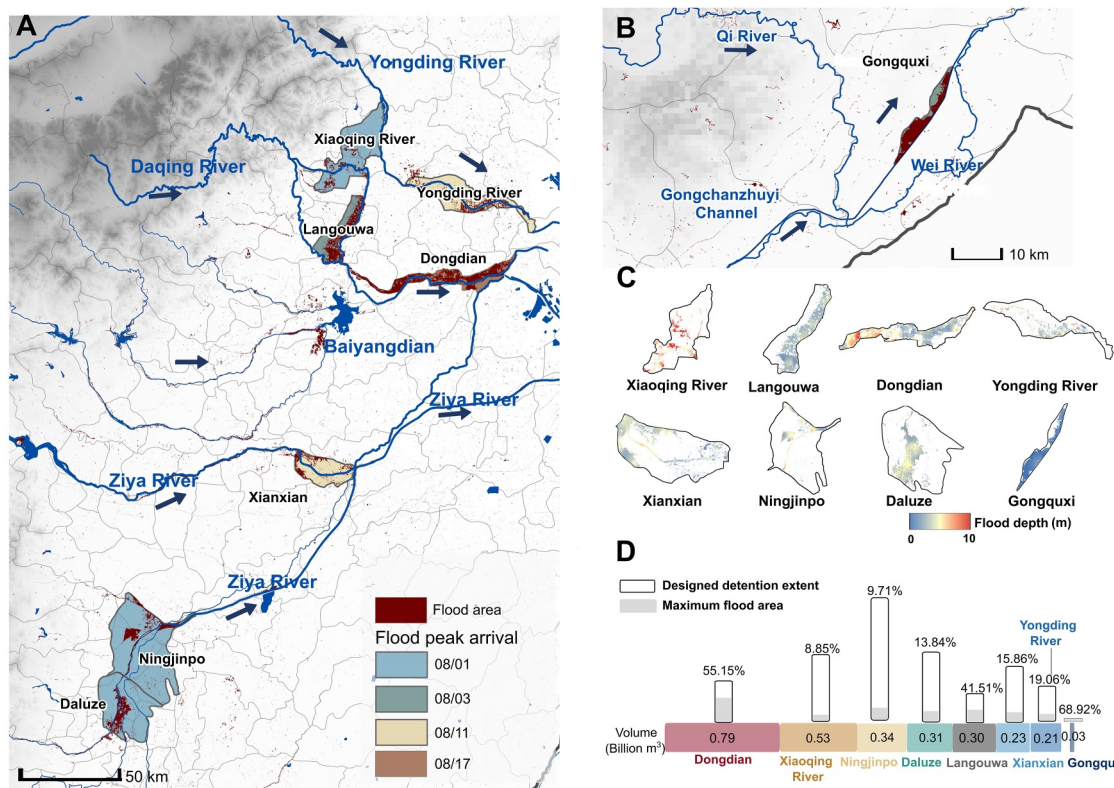


Figure 4. The 3D flood structure and the derived flood detention volume time-series. (a–b) The maximum flood extent of activated FDAs. The blue arrows adjacent to the primary rivers indicate the direction of flow. (c) The flood depth maps of eight FDAs during flood peaks. (d) The maximum flood extent and the maximum flood detention volume of each FDA.

3.2. Flood Detention Volume of 2.74 Billion m³

To highlight the critical role of FDAs in such flood control system, we further conducted a quantitative assessment of the FDAs' flood-control effectiveness through the constructed 3D flood structure. In terms of flooded extent, our explicit pixel-level analysis revealed that the floodwaters were entirely held within the FDAs, without any overflow to the surroundings (Figures 4a and 4b). Although the eight activated FDAs comprise only 1.26% of HRB's terrain, they account for 33.2% of the total flood extent. Specifically, 68.9% of the area of Gongquxi FDA, 55.2% of Dongdian FDA, and 41.5% of Langouwa FDA were flooded. On the other hand, only 8.9% of the area of Yongding River FDA and 13.8% of Daluze FDA were flooded.

In terms of the maximum flood detention volume, the total capacity of the eight FDAs amounted to 2.74 billion m³, comparable to 2.85 billion m³ held by the 84 large- and medium-sized reservoirs in the upstream areas of the HRB. The Dongdian FDA held the largest flood detention volume (790 million m³), accounting for 27.7% of the total detention volume. This is attributed to Dongdian FDA's strategic location downstream of the Daqing River, a major conduit for floodwaters. Xiaoqing River FDA is the second largest in detention volume (530 million m³), accounting for 19.63% of the total detention volume. Despite its relatively small flood extent, the Xiaoqing River FDA sits in the transition zone between mountains and plains, featuring a pronounced topographic relief. As a result, floodwaters in this area reached depths exceeding 10 m (Figure 4c). The Gongquxi FDA held the least flood detention volume (30 million m³) due to its small dimensions (Figure 4d).

3.3. Rapid Floodwater Drainage

The estimated $D_{0.8}$ values of most FDAs were less than two weeks. One sole exception occurred at the Dongdian FDA with the longest time to drain floodwaters and a $D_{0.8}$ of 34 days. On the contrary, the Gongquxi and Yongding River FDAs had the shortest drainage with $D_{0.8}$ of 5 and 6 days, respectively. Interestingly, despite the

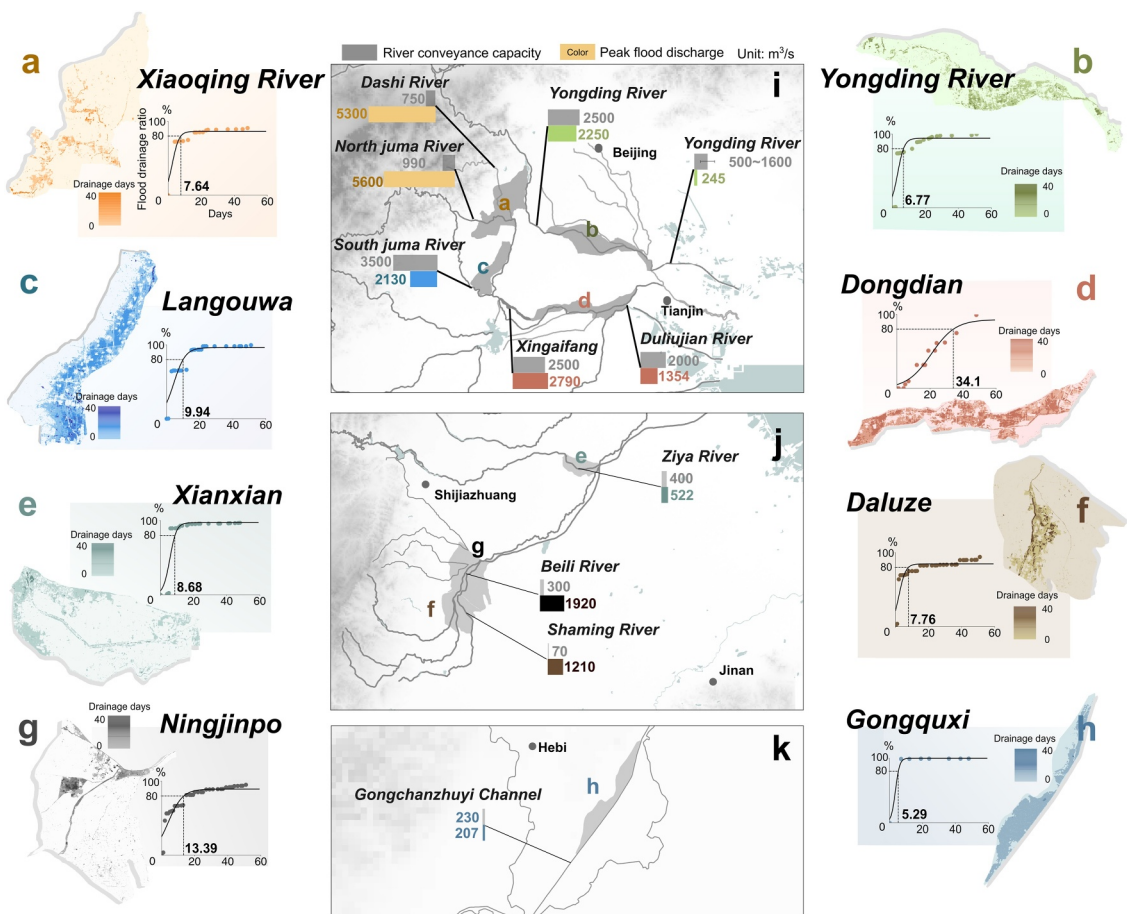


Figure 5. Floodwater drainage processes of FDAs. (a–h) Pixel-level flood drainage duration of activated FDAs. Floodwater drainage processes characterized by the Cumulative Distribution Function (CDF) fitted with a logistic function. Days required for 80% of the flood extent drainage have been labeled. (i–k) River conveyance capacity and the peak flood discharge during this event, in the unit of m^3/s .

Dongdian FDA experiencing the most significant flood extent and flood detention volume, the drainage timeline was sufficient to accommodate the standard winter wheat sowing scheduled for October 2023 (Figures 5a–5h).

4. Discussion

4.1. Driving Factor of the Flood Drainage

Most of the detained floodwaters were directed into low-lying natural rivers or manmade channels within the FDAs and subsequently transported out. The drainage mechanism suggests that the conveyance capacities of these rivers and channels are critical driving factors in the flood drainage process. To obtain quantitative evidence supporting the hypothesis, we adopted the conveyance capacities (Du et al., 2023) and quantified the flood drainage capacities of each FDA to examine their correlation (Figures 5i–5k). Here, flood drainage capacity was quantified as the ratio of the maximum flooded area to the total FDA area, divided by the drainage duration ($D_{0.8}$) (Figure 6), with larger values indicating relatively higher capacities. The results showed that Gongquxi and Langouwa FDAs had the highest drainage capacities (13.19 and 4.17, respectively), whereas Daluze, Ningjinpo, Dongdian, and Xiaoqing River FDAs exhibited comparatively lower capacities, ranging from 0.72 to 1.78.

A strong correlation between flood drainage capacities and river conveyance capacities was observed and therefore proved the critical role of conveyance capacity during flood drainage process. The FDAs with enhanced drainage capacities tend to exhibit greater river conveyance capacities. For instance, the Gongquxi and Langouwa FDAs show exceptionally strong flood drainage capacities. Although Gongquxi and Langouwa FDAs experienced significant flooding (68.9% and 41.5% of their respective total areas), it required only 5 and 6 days,

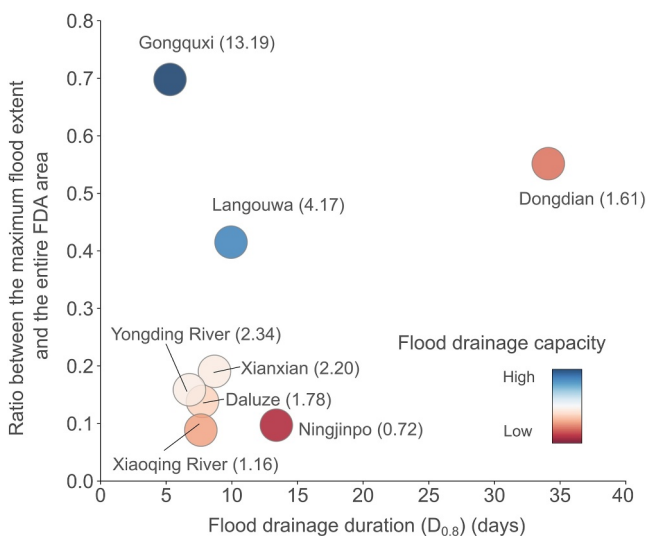


Figure 6. The flood drainage capacities of FDAs. The labeled values indicate the quantified flood drainage capacities.

mining and tailings deposition in North Juma River have led to sediment accumulation and riverbank instability, reducing the conveyance capacities (Hackney et al., 2020; Lauer & Parker, 2008). As a result, the Daluze, Ningjinpoo, and Xiaoqing River FDAs possessed river conveyance capacity limited to hundreds of cubic meters per second, rendering them inadequate for managing large-scale floods from upstream, which can occur at rates of thousands of cubic meters per second (Figures 5i and 5j). Although the river conveyance capacity of the Dongdian FDA was only slightly lower than its flood peak, cascade effects—such as delayed drainage and backwater effects, as discussed in the next section—explained its relatively slow flood drainage.

4.2. Cascade Effects of FDAs

Besides estimating the floodwater detention volume and drainage duration of FDAs, the recovered lifespan of 3D flood structure, integrating flood extent and depth, offers valuable insights into FDA characteristics and management. Flood detention volume time-series could be derived and visually illustrates the dynamic process of each FDAs from activation to the near-completion of water drainage. The time series revealed apparent disparities in flood detention processes among the upstream and downstream FDAs. Upstream FDAs (e.g., Daluze, Ningjinpoo, and Xiaoqing River) were activated early around July 30, and reached brief flood peaks by August 1. In contrast, downstream FDAs—Langouwa, Xianxian, Yongding River, and Dongdian—exhibited later and more prolonged flood peaks. In particular, the Dongdian FDA exhibited extremely longer flood duration and higher flood peaks compared to other FDAs (Figure 7).

To investigate the causes of differences between upstream and downstream FDAs, we collected discharge time series from major hydrological stations at the inlets and outlets of the FDAs and nearby reservoirs. Based on the data, we estimated outflow discharges under the assumption that the FDAs were absent and compared these estimates with actual outflow records. Without the FDA's flood detention effect, the outflow discharge was approximated as the sum of the major rivers entering the area. To account for travel time, each river's discharge was adjusted by adding its propagation time from the inlet hydrological station to the outlet station, as provided by the China's water authorities. For example, without the Langouwa FDA, the outflow at Xingaifang Station was calculated as the sum of the Baigou River discharge from Dongci Station and the South Juma River discharge from Beihedian Station, adjusted for propagation times of 9 and 7 hr, respectively (Figure 8a).

The comparison results and discharge time series revealed that these differences were driven by cascade effects—including delayed drainage, cumulative loading, and backwater—occurring between sequential FDAs and in conjunction with other flood control infrastructure. Delayed drainage effects between upstream FDAs or reservoirs and downstream FDAs resulted in prolonged flood peaks in the downstream FDAs. For instance, the prolonged flood peak in Langouwa FDA was caused by delayed drainage from its upstream Xiaoqing River FDA.

respectively, for 80% of the floodwaters to be removed (Figure 5). The high drainage capacities of Gongquxi and Langouwa FDAs can be linked to considerable conveyance capacities of primary rivers intersecting with them, which have been improved through river dredging initiatives and the construction of artificial channels in HRB. In Gongquxi, the manmade Gongchanzhuyi Channel (Figure 5k) reached a conveyance capacity of $\sim 230 \text{ m}^3/\text{s}$ after the dredging and management projects in 2018, surpassing the peak flood discharge of $207 \text{ m}^3/\text{s}$. Similarly, in Langouwa, the primary channel of the South Juma River has a conveyance capacity of $3,500 \text{ m}^3/\text{s}$, exceeding the peak flood discharge of $2,130 \text{ m}^3/\text{s}$. Moreover, the manmade Xingaifang floodway directed floodwaters into the Dongdian FDA (Figure 5i).

In contrast, the Daluze, Ningjinpoo, Xiaoqing River, and Dongdian FDAs were limited in flood drainage capacities in this event. With only 9.71% of areas being flooded, Ningjinpoo required nearly two weeks to drain 80% of the floodwaters (Figure 5). The limited drainage capacities of the Daluze, Ningjinpoo, and Xiaoqing River FDAs stem from the low river conveyance capacities. The surrounding mountains and plains create significant variations in channel width between upstream and downstream areas. The narrow downstream channels could not accommodate the large floods originating from the expansive upstream channels. Furthermore, the lack of regulation in sand

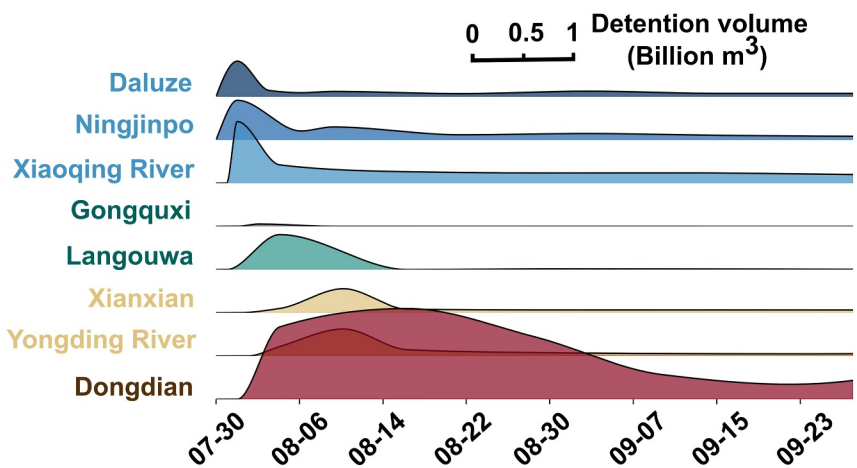


Figure 7. Time-series flood detention volume of each FDA.

By detaining substantial floodwaters, the Xiaoqing River FDA reduced the flood peak from $\sim 6,000 \text{ m}^3/\text{s}$ to $\sim 2,000 \text{ m}^3/\text{s}$, then gradually released these floodwaters to Langouwa FDA—extending the drainage duration from about two days to over five days and producing a lower but much longer flood peak (Figures 8a and 8e). Furthermore, compounded delayed drainage from two sequential upstream FDAs—the Xiaoqing River FDA and the Langouwa FDA—produced an exceptionally long flood peak of nearly one month in the Dongdian FDA (Figures 8a and 8d). For Xianxian FDA and Yongding River FDA without upstream FDAs, the prolonged flood peaks originated from upstream reservoirs. In the Xianxian FDA, the Guannan and Huangbizhuang reservoirs stored most floodwaters. After reaching design limits, the Huangbizhuang Reservoir gradually released water, prolonging the flood peak (Figures 8b and 8f). Upstream of the Yongding River FDA, two sequential reservoirs—the Da'ning Reservoir and the Yongding River Reservoir—also delayed the drainage of floodwaters, resulting in a prolonged flood peak (Figure 8a).

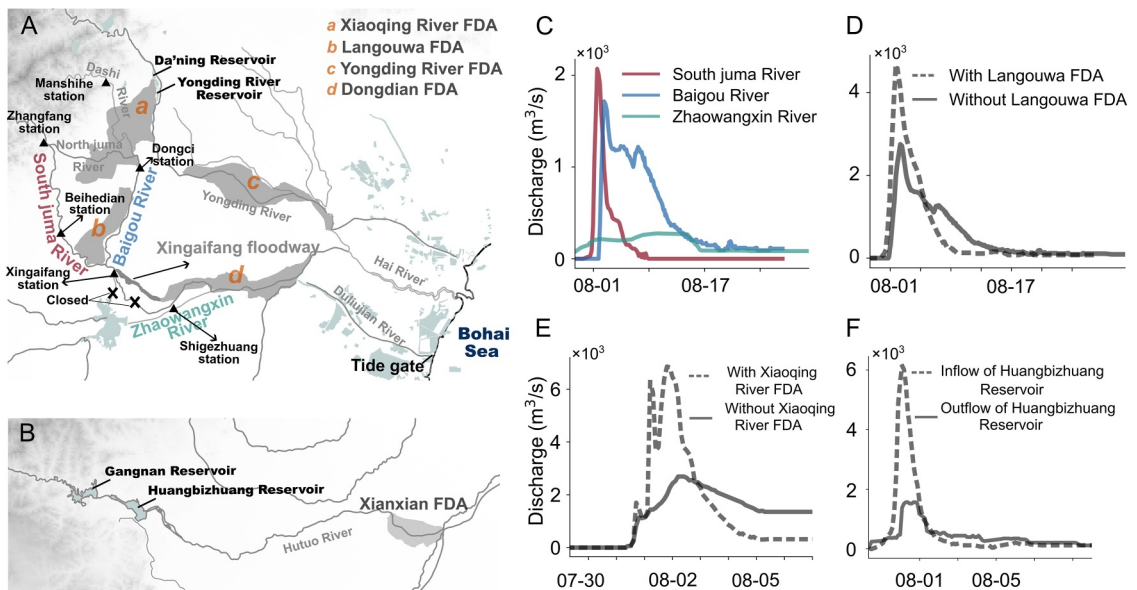


Figure 8. The cascade effects between FDAs and other flood control infrastructures. (a–b) Spatial arrangement of FDAs along river systems and reservoirs. (c) The discharges of the three major rivers flowing into the Dongdian FDA. (d) Observed and estimated discharges (with and without the Langouwa FDA, respectively) before entering the Dongdian FDA. (e) Observed and estimated discharges (with and without the Xiaoqing River FDA, respectively) before entering the Langouwa FDA. (f) Inflow and outflow discharge of Huangbizhuang reservoir located on upstream of Xianxian FDA.

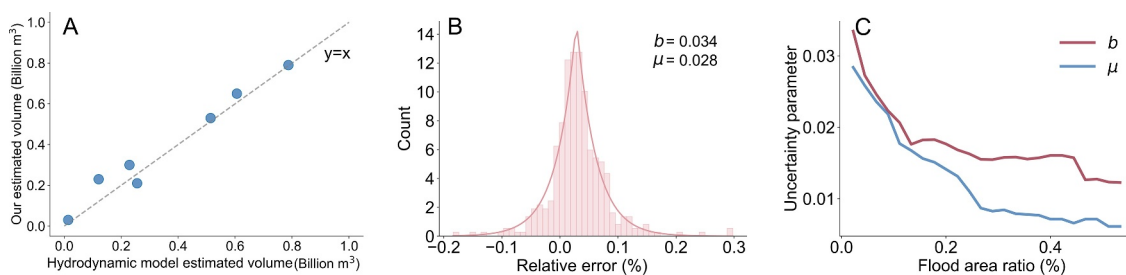


Figure 9. Model validation and uncertainty qualification. (a) Comparison between our estimated maximum flood detention volume and the hydrodynamic model results reported by Du et al. (2023). (b) Systematic bias μ and uncertainty scale b of the predicted flood area at flood area ratio threshold of 2%. (c) Variation of the model's uncertainty and bias with different flood-area ratio thresholds.

Besides the delayed drainage effects, the abnormally long and high flood peak in the Dongdian FDA was also driven by cumulative loading and backwater effects. It received floodwaters from three major rivers (i.e., Baigou River, South Juma River, and Zhaowangxin River) that converged flows from several upstream rivers and FDAs. The Baigou River carried the outflows from the Langouwa and Xiaoqing River FDAs. Moreover, with the natural river channel that once directed floods to the Baiyangdian wetland closed, all floodwaters from the South Juma River and the Baigou River poured into the Dongdian FDA without attenuation. The cumulative loading effects led to the extremely high flood peak in Dongdian FDA (Figures 8a and 8c). Additionally, to avoid the backwater effects of the Bohai Sea, the tide gate on the Dulinjian River was opened and closed twice daily, further prolonged flood drainage duration of Dongdian FDA (Figure 8a).

Depending on the specific characteristics, distinct management strategies are necessary for FDAs in different locations. For upstream FDAs, the brief interval between the onset of heavy rainfall and the arrival of floodwaters places significant demands on the efficiency of activation decisions, evacuation notices and organizations. This highlights the critical need for well-structured evacuation plans and thorough pre-disaster drills to ensure timely and effective responses in these regions. In contrast, although the downstream FDAs have relatively longer preparation times, their overall activation durations are extended, necessitating prolonged accommodation and assistance for relocated residents.

4.3. Model Validation and Uncertainty Analysis

Our model validation results indicated that the recovered 3D flood structure was accurate. The flood extent showed strong agreement with the ground truth, achieving an average MIoU of 88.34%. Moreover, our estimated maximum flood detention volume closely matched that derived from a hydrodynamic model. Since the volume was calculated from both flood extent and depth, and the extent had already been verified as accurate, this agreement indicated that the estimated flood depth was also reliable (Figure 9a).

The relative error of the predicted flood area shows a systematic bias of 0.028, indicating a slight overestimation to flood areas. This overestimation arose from misclassifying mountainous shadow areas with low backscatter values as flooded areas. With an uncertainty scale of 0.034 (Figure 9b), the 95% confidence interval for the actual flood area was given by:

$$A \in \left[0.85\hat{A}, 1.10\hat{A} \right] \quad (4)$$

Additionally, both the systematic bias and the uncertainty scale declined with increasing flood-area ratio, suggesting that in more severely flood regions, our model yielded flood area estimates with less bias and uncertainty (Figure 9c).

Given the generalizability of the FwDET uncertainty pattern (Teng et al., 2022), we adopted the pattern as a reference for assessing the uncertainty of our flood-depth estimates. Based on Laplace distribution fitting of 10,000 samples across 26 flood scenes, Teng et al. (2022) reported a bias of 0.32 m and an uncertainty of 0.58 m for FwDET, from which a confidence interval can also be derived. The positive bias indicated that FwDET tended to underestimate flood depth. This underestimation arose from combining flood extents derived from multi-

source remote sensing imagery with DEM data. When the mapped flood extent did not align with the DEM elevations, some internal pixels of the flood extent polygons were incorrectly assigned lower floodwater elevations referring to nearer boundaries, rather than the actual higher elevations from the maximum reach of floodwaters, leading to an underestimation of floodwater depth.

4.4. Broader Applicability of 3D Flood Reconstruction Approach

Although we applied the 3D flood reconstruction approach only to the 2023 flood in HRB, its algorithmic generalizability and the availability of core data make it broadly applicable to other flood events. The extracted flood extent demonstrated strong generalizability across different times, locations, and sensors, while FwDET shown stable performance across a wide range of flood events (Teng et al., 2022). Although we adopted multi-source remote sensing imagery, including some commercial satellite data, the essential data sets for reconstructing the lifespan of 3D flood structure were the globally available and freely accessible Sentinel-1 SAR, Sentinel-2 optical images, and Copernicus DEM GLO-30 corrected by ASF. Sentinel-1 with a 12-day revisit interval (when a single satellite is in use, interval is shortened by half with twin satellites) was sufficient for capturing the dynamic flood extent, while any flood peaks missed due to this relatively long interval could be supplemented by Sentinel-2 optical imagery. Commercial satellites such as Gaofen-3 and Lutan-1 were used solely to further increase temporal resolution of the dynamic flood extent. Their absence would merely reduce the temporal density of the flood extent time series without altering the overall trend of the reconstructed flood extent.

Therefore, when applying this approach to other flood events, the optimal strategy is to integrate as many multi-source SAR images as possible to improve temporal resolution. If the supplementary SAR images are dual-polarized, they can be incorporated into the deep learning model due to its strong generalizability across multiple sensors. If they are single-polarized, the Otsu thresholding method can be used to extract the flood extent. Notably, when the additional SAR images have a coarser resolution than the 10-m resolution DEM, the accuracy of the retrieved flood depth may decrease slightly (Teng et al., 2022). When additional SAR imagery is unavailable, Sentinel-1 SAR and Sentinel-2 optical images are sufficient to capture the overall trends, albeit with limited temporal resolution, and will not cause a qualitative change in the final 3D flood structure.

4.5. Envisions About FDA Potentials

Vast areas such as India, Bangladesh, Pakistan, and some other Asian countries possess extensive flood-prone areas and face significant agricultural demands to sustain their large populations, which is similar to the circumstances in China. However, FDA constructions are either at its early stages or have not yet been planned in these developing countries (Gupta, 2020; Rahman & Salehin, 2013; Tariq & Van De Giesen, 2012). Building on robust evidence of FDA effectiveness in flood control and drainage, the HRB FDA model holds significant potential for adoption in these countries, promising substantial flood mitigation and loss reduction.

Beyond their flood control effectiveness, we envision the ecological and socioeconomic benefits that FDAs can deliver. First, FDAs can alleviate droughts by floodwater resources. Studies have shown the groundwater level elevation underneath the FDAs (Lan et al., 2024). Additionally, FDAs, with flood detention capacities comparable to reservoirs, can permanently retain detained floodwaters in lakes, rivers, and low-lying areas (Ding et al., 2015; Wang et al., 2023). This approach is especially beneficial for countries like China, India, and Bangladesh, who face the dual threats of floods and droughts due to irregular rainfall distribution. Second, FDAs enhance the ecosystem services (Dottori et al., 2023). Countries like the Netherlands, Germany, and China have initiated pilot projects to establish wetland parks in FDAs (Schindler et al., 2016; Wang, 2024). These projects aim to reestablish the connection between rivers and their degraded floodplains, restoring their natural functions while also promoting biodiversity recovery, improving water purification, and regulating sediment flow (Kail et al., 2015). Meanwhile, wetland parks offer recreational and scenic values and can boost the tourism revenue.

4.6. Limitation and Future Work

Despite the reliability and broad application of the recovered 3D flood structure, certain limitations remain in our approach due to algorithmic shortcomings and data constraints. Errors persisted in both flood extent and depth estimation. In SAR imagery, the high morphological similarity between mountainous shadows and flooded areas introduced artifacts into the predicted flood extent, leading to overestimation of flood area. And mismatches between DEM data and flood extents derived from multi-source remote sensing imagery introduced notable

uncertainties in flood depth. Additionally, lack of in situ observations and input data required for hydrodynamic models prevented us from conducting a comprehensive validation and case-specific uncertainty analysis of the estimated flood depth.

In the future, the performance of the deep learning algorithm for extracting flood extent can be improved by incorporating a larger and more diverse training samples, as well as adopting more advanced model architectures. For flood-depth reconstruction, the mismatch between elevation and flood extent can be alleviated by using DEM data with higher resolution and accuracy. We also call for the data sharing of high-resolution DEM data in critical catchments and in situ flood-depth observations, which are essential for enhancing algorithm performance and enabling more rigorous assessment on their errors and uncertainties.

5. Conclusion

By reconstructing the 3D flood structure during a catastrophic flood event, our study quantitatively demonstrated the pivotal role of FDAs in flood management systems, revealing a total flood detention volume of 2.74 billion m³. Most of the detained floodwaters were drained within two weeks, enabling the prompt recovery of agricultural activities and community livelihoods. Additionally, the lifespan of the 3D flood structure revealed the critical role of river conveyance capacities during flood drainage process and pronounced disparities in flood detention processes between upstream and downstream FDAs due to cascade effects, providing critical insights to guide the activation timing and management of FDA. This study responds to longstanding controversies surrounding FDAs by providing quantitative evidence of their significant benefits in flood control and drainage, thereby enhancing understanding of modern flood-control systems, and supporting their construction and global adoption, particularly in flood-prone regions of developing and underdeveloped countries.

Conflict of Interest

The authors declare no conflicts of interest relevant to this study.

Data Availability Statement

Sentinel-1 SAR images used for extracting pre-flood water bodies and two-month flood extent across the Hai River Basin, as well as the Copernicus DEM GLO-30 corrected by Alaska Satellite Facility data for flood depth recovery, are available in the in-text data citation references: OPERA (2023). The Gaofen-3 and Lutan-1 data used for flood extent mapping are not publicly available due to their commercial use restrictions. These data are however available from the authors upon reasonable request and with permission of Land Satellite Remote Sensing Application Center. The land use data, the 1-km resolution Grid GDP data, and the population data used for landuse analysis over the Flood Detention Areas are available in the in-text data citation references: Karra et al. (2021), Wang and Wang (2022), and WorldPop & Center for International Earth Science Information Network (CIESIN), Columbia University (2018), respectively. We have preserved our codes and generated data for this study in Zenodo (Lin & Hu, 2024).

Acknowledgments

We thank China's Resource and Environmental Science Platform for offering Gaofen-3 and Lutan-1 satellite images. This work was supported by the Distinguished Young Scholars of the National Natural Science Foundation of China (Overseas), Beijing Natural Science Foundation (8252007), and State Key Laboratory of Hydraulics and Mountain River Engineering (SKHL2406).

References

- Al-Ali, Z., Abulibdeh, A., Al-Awadhi, T., Mohan, M., Nasiri, N. A., Al-Barwani, M., et al. (2024). Examining the potential and effectiveness of water indices using multispectral sentinel-2 data to detect soil moisture as an indicator of mudflow occurrence in arid regions. *International Journal of Applied Earth Observation and Geoinformation*, 130, 103887. <https://doi.org/10.1016/j.jag.2024.103887>
- Alfieri, L., Feyen, L., & Di Baldassarre, G. (2016). Increasing flood risk under climate change: A Pan-European assessment of the benefits of four adaptation strategies. *Climatic Change*, 136(3–4), 507–521. <https://doi.org/10.1007/s10584-016-1641-1>
- Andrew, O., Apan, A., Paudyal, D. R., & Perera, K. (2023). Convolutional neural network-based deep learning approach for automatic flood mapping using NovaSAR-1 and Sentinel-1 data. *ISPRS International Journal of Geo-Information*, 12(5), 194. <https://doi.org/10.3390/ijgi12050194>
- Ansari, A. H., Mejia, A., & Cibin, R. (2024). Flood teleconnections from levees undermine disaster resilience. *npj Natural Hazards*, 1(1), 2. <https://doi.org/10.1038/s44304-024-00002-1>
- Arrighi, C., Rossi, L., Trasforini, E., Rudari, R., Ferraris, L., Brugioni, M., et al. (2018). Quantification of flood risk mitigation benefits: A building-scale damage assessment through the RASOR platform. *Journal of Environmental Management*, 207, 92–104. <https://doi.org/10.1016/j.jenvman.2017.11.017>
- Barbour, E. J., Adnan, M. S. G., Borgomeo, E., Paprocki, K., Khan, M. S. A., Salehin, M., & Hall, J. W. (2022). The unequal distribution of water risks and adaptation benefits in coastal Bangladesh. *Nature Sustainability*, 5(4), 294–302. <https://doi.org/10.1038/s41893-021-00846-9>
- Barker, J. (2013). Environmental groups and Cairo, Ill., officials urge EPA to veto new Madrid levee. *St. Louis Post-Dispatch*. Retrieved from https://www.stltoday.com/business/local/environmental-groups-and-cairo-ill-officialsurge-epa-tovetoto/article_5c61d503-2cd0-5b98-9af5-0b7514f6baea.html

- Buechel, M., Slater, L., & Dadson, S. (2022). Hydrological impact of widespread afforestation in Great Britain using a large ensemble of modelled scenarios. *Communications Earth & Environment*, 3(1), 6. <https://doi.org/10.1038/s43247-021-00334-0>
- Chan, N. W., Ghani, A. A., Samat, N., Hasan, N. N. N., & Tan, M. L. (2019). Integrating structural and non-structural flood management measures for greater effectiveness in flood loss reduction in the Kelantan river Basin, Malaysia. In *Paper presented at proceedings of the AWAM international conference on civil engineering 2019 (AICCE'19)*. Springer. Penang, Malaysia. https://doi.org/10.1007/978-3-030-32816-0_87
- Chen, L., Zhu, Y., Papandreou, G., Schroff, F., & Adam, H. (2018). Encoder-decoder with atrous separable convolution for semantic image segmentation. In *Paper presented at proceedings of the European conference on computer vision (ECCV)*. EACV. Munich, Germany. https://doi.org/10.1007/978-3-030-01234-2_49
- Cohen, S., Brakenridge, G. R., Kettner, A., Bates, B., Nelson, J., McDonald, R., et al. (2017). Estimating floodwater depths from flood inundation maps and topography. *Journal of the American Water Resources Association*, 54(4), 847–858. <https://doi.org/10.1111/jwr.12609>
- Cohen, S., Peter, B. G., Haag, A., Munasinghe, D., Moragoda, N., Narayanan, A., & May, S. (2022). Sensitivity of remote sensing floodwater depth calculation to boundary filtering and digital elevation model selections. *Remote Sensing*, 14(21), 5313. <https://doi.org/10.3390/rs14215313>
- Development Research Center of the Ministry of Water Resources (DRC). (2022). Research on issues and measures for the construction and management of flood detention areas in China. Retrieved from https://www.waterinfo.com.cn/xsyj/tszs/20220809_34722.html
- Ding, W., Zhang, C., Peng, Y., Zeng, R., Zhou, H., & Cai, X. (2015). An analytical framework for flood water conservation considering forecast uncertainty and acceptable risk. *Water Resources Research*, 51(6), 4702–4726. <https://doi.org/10.1002/2015wr017127>
- Dottori, F., Mentaschi, L., Bianchi, A., Alfieri, L., & Feyen, L. (2023). Cost-effective adaptation strategies to Rising River flood risk in Europe. *Nature Climate Change*, 13(2), 196–202. <https://doi.org/10.1038/s41558-022-01540-0>
- Du, X., He, B., Xu, W., Zhang, M., & Yuan, D. (2023). Retrospective operation in the “23·7” extreme flood storage and detention area of the Hai river basin and reflection on systematic governance and green development. *China Flood & Drought Management*, 33, 31–38. (In Chinese).
- Galelli, S., Dang, T. D., Ng, J. Y., Chowdhury, A. F. M. K., & Arias, M. E. (2022). Opportunities to curb hydrological alterations via dam re-operation in the Mekong. *Nature Sustainability*, 5(12), 1058–1069. <https://doi.org/10.1038/s41893-022-00971-z>
- Grafton, Q., Daniell, K. A., Nauges, C., Rinaudo, J., & Chan, N. W. W. (2015). *Understanding and managing urban water in transition*. Springer. Netherlands. <https://doi.org/10.1007/978-94-017-9801-3>
- Grill, G., Lehner, B., Thieme, M., Geenen, B., Tickner, D., Antonelli, F., et al. (2019). Mapping the world's free-flowing rivers. *Nature*, 569(7755), 215–221. <https://doi.org/10.1038/s41586-019-1111-9>
- Grimaldi, S., Xu, J., Li, Y., Pauwels, V., & Walker, J. (2019). Flood mapping under vegetation using single SAR acquisitions. *Remote Sensing of Environment*, 237, 111582. <https://doi.org/10.1016/j.rse.2019.111582>
- Gupta, K. (2020). Challenges in developing urban flood resilience in India. *Philosophical Transactions of the Royal Society A*, 378(2168), 20190211. <https://doi.org/10.1098/rsta.2019.0211>
- Hackney, C. R., Darby, S. E., Parsons, D. R., Leyland, J., Best, J. L., Aalto, R., et al. (2020). River bank instability from unsustainable sand mining in the lower Mekong River. *Nature Sustainability*, 3(3), 217–225. <https://doi.org/10.1038/s41893-019-0455-3>
- Hai River Chronicles Compilation Committee. (1997). The chronicles of the Hai River. China: Water resources and hydropower press.
- Han, J., Zhang, Z., Xu, J., Chen, Y., Jägermeyr, J., Cao, J., et al. (2024). Threat of low-frequency high-intensity floods to global cropland and crop yields. *Nature Sustainability*, 7(8), 994–1006. <https://doi.org/10.1038/s41893-024-01375-x>
- Jiang, X., Liang, S., He, X., Ziegler, A. D., Lin, P., Pan, M., et al. (2021). Rapid and large-scale mapping of flood inundation via integrating spaceborne synthetic aperture radar imagery with unsupervised deep learning. *ISPRS Journal of Photogrammetry and Remote Sensing*, 178, 36–50. <https://doi.org/10.1016/j.isprsjprs.2021.05.019>
- Kail, J., Brabec, K., Poppe, M., & Januschke, K. (2015). The effect of river restoration on fish, macroinvertebrates and aquatic macrophytes: A meta-analysis. *Ecological Indicators*, 58, 311–321. <https://doi.org/10.1016/j.ecolind.2015.06.011>
- Karra, K., Kontgis, C., Statman-Weil, Z., Mazzariello, J. C., Mathis, M., & Brumby, S. P. (2021). Sentinel-2 10m land use/land cover time series of the world [Dataset]. *Microsoft Planetary Computer*, 4704–4707. <https://doi.org/10.1109/igars47720.2021.9553499>
- Kind, J., Botzen, W. W., & Aerts, J. C. (2016). Accounting for risk aversion, income distribution and social welfare in cost-benefit analysis for flood risk management. *Wiley Interdisciplinary Reviews: Climate Change*, 8(2), e446. <https://doi.org/10.1002/wcc.446>
- Kreibich, H., Van Loon, A. F., Schröter, K., Ward, P. J., Mazzoleni, M., Sairam, N., et al. (2022). The challenge of unprecedented floods and droughts in risk management. *Nature*, 608(7921), 80–86. <https://doi.org/10.1038/s41586-022-04917-5>
- Lan, Q., Dong, J., Lai, S., Wang, N., Zhang, L., & Liao, M. (2024). Flood inundation extraction and its impact on ground subsidence using Sentinel-1 data: A case study of the “7·20” rainstorm event in Henan province, China. *Ieee Journal of Selected Topics in Applied Earth Observations and Remote Sensing*, 17, 2927–2938. <https://doi.org/10.1109/jstars.2023.3348845>
- Lauer, J. W., & Parker, G. (2008). Modeling framework for sediment deposition, storage, and evacuation in the floodplain of a meandering river: Application to the Clark Fork River, Montana. *Water Resources Research*, 44(8), W08404. <https://doi.org/10.1029/2006wr005529>
- Liang, W., Carberry, P., Wang, G., Lü, R., Lü, H., & Xia, A. (2011). Quantifying the yield gap in wheat-maize cropping systems of the Hebei Plain, China. *Field Crops Research*, 124(2), 180–185. <https://doi.org/10.1016/j.fcr.2011.07.010>
- Lin, F., Hu, X., Lin, Y., Li, Y., Liu, Y., & Li, D. (2024). Dual-branch multi-modal convergence network for crater detection using chang'e image. *International Journal of Applied Earth Observation and Geoinformation*, 134, 104215. <https://doi.org/10.1016/j.jag.2024.104215>
- Lin, Y., & Hu, X. (2024). Yiling Lin 0610/2023-Hai-River-Flood-Mapping: HRB_flood [Dataset]. Zenodo. <https://doi.org/10.5281/zenodo.1454349>
- Lin, Y., Hu, X., Lu, H., Niu, F., Liu, G., Huang, L., et al. (2025). Multi-annual inventorying of retrogressive thaw slumps using domain adaptation. *Journal of Geophysical Research Machine Learning and Computation*, 2(1), e2024jh000370. <https://doi.org/10.1029/2024jh000370>
- Merz, B., Blöschl, G., Vorogushyn, S., Dottori, F., Aerts, J. C. H., Bates, P., et al. (2021). Causes, impacts and patterns of disastrous river floods. *Nature Reviews Earth & Environment*, 2(9), 592–609. <https://doi.org/10.1038/s43017-021-00195-3>
- Morton, L. W., & Olson, K. R. (2013). Birds point-new Madrid floodway: Redesign, reconstruction, and restoration. *Journal of Soil and Water Conservation*, 68(2), 35A–40A. <https://doi.org/10.2489/jswc.68.2.35a>
- Munoz, S. E., Giosan, L., Therrell, M. D., Remo, J. W. F., Shen, Z., Sullivan, R. M., et al. (2018). Climatic control of Mississippi River flood hazard amplified by river engineering. *Nature*, 556(7699), 95–98. <https://doi.org/10.1038/nature26145>
- Nittrouer, J. A., Best, J. L., Brantley, C., Cash, R. W., Czapiga, M., Kumar, P., & Parker, G. (2012). Mitigating land loss in coastal Louisiana by controlled diversion of Mississippi River sand. *Nature Geoscience*, 5(8), 534–537. <https://doi.org/10.1038/ngeo1525>
- Olson, K. R., & Morton, L. W. (2013). Restoration of 2011 flood-damaged birds point-new Madrid floodway. *Journal of Soil and Water Conservation*, 68(1), 13A–18A. <https://doi.org/10.2489/jswc.68.1.13a>
- OPERA. (2023). OPERA level-2 radiometric terrain corrected from Sentinel-1 [Dataset]. NASA Alaska Satellite Facility Distributed Active Archive Center. https://doi.org/10.5067/SNWG/OPERA_L2_RTC-S1_V1

- Opperman, J. J., Galloway, G. E., Fargione, J., Mount, J. F., Richter, B. D., & Secchi, S. (2009). Sustainable floodplains through large-scale reconnection to rivers. *Science*, 326(5959), 1487–1488. <https://doi.org/10.1126/science.1178256>
- Otsu, N. (1979). A threshold selection method from gray-level histograms. *IEEE Transactions on Systems, Man, and Cybernetics*, 9(1), 62–66. <https://doi.org/10.1109/tsmc.1979.4310076>
- Pearcy, M. T. (1996). *A history of the Mississippi River commission, 1879–1928: From levees-only to a comprehensive program of flood control for the lower Mississippi Valley*. University of North Texas. Denton, TX.
- Rahman, R., & Salehin, M. (2013). *Disaster risk reduction. Flood risks and reduction approaches in Bangladesh* (pp. 65–90). Springer. Tokyo. https://doi.org/10.1007/978-4-431-54252-0_4
- Schindler, S., O'Neill, F. H., Biró, M., Damm, C., Gasso, V., Kanka, R., et al. (2016). Multifunctional floodplain management and biodiversity effects: A knowledge synthesis for six European countries. *Biodiversity & Conservation*, 25(7), 1349–1382. <https://doi.org/10.1007/s10531-016-1129-3>
- Serra-Llobet, A., Kondolf, G. M., Magdaleno, F., & Keenan-Jones, D. (2021). *Flood diversions and bypasses: Benefits and challenges* (Vol. 9(1), e1562). Wiley Interdisciplinary Reviews Water. <https://doi.org/10.1002/wat2.1562>
- State Ministry of the Environment Baden-Württemberg. (2007). The Integrated Rhine programme—flood control and restoration of former floodplains along the Upper Rhine. Retrieved from https://rp.baden-wuerttemberg.de/fileadmin/RP-Internet/Themenportal/Wasser_und_Boden/Integriertes_Rheinprogramm/_DocumentLibraries/Rueckhalterraum/irp-en.pdf
- Tariq, M. A. U. R., & Van De Giesen, N. (2012). Floods and flood management in Pakistan. *Physics and Chemistry of the Earth/Physics and Chemistry of the Earth*, 47, 11–20. Parts A/B/C. <https://doi.org/10.1016/j.pce.2011.08.014>
- Teng, J., Penton, D. J., Ticehurst, C., Sengupta, A., Freebairn, A., Marvanek, S., et al. (2022). A comprehensive assessment of floodwater depth estimation models in semiarid regions. *Water Resources Research*, 58(11), e2022WR032031. <https://doi.org/10.1029/2022wr032031>
- Tiampo, K. F., Huang, L., Simmons, C., Woods, C., & Glasscoe, M. T. (2022). Detection of flood extent using sentinel-1A/B synthetic aperture radar: An application for Hurricane Harvey, Houston, TX. *Remote Sensing*, 14(9), 2261. <https://doi.org/10.3390/rs14092261>
- Van Doorn-Hoekveld, W., & Groothuijse, F. (2014). Challenge in implementation flood storage areas in the UK. In *Paper presented at 6th international conference on flood management. Brazil*.
- Van Doorn-Hoekveld, W., & Groothuijse, F. (2017). Analysis of the strengths and weaknesses of Dutch water storage areas as a legal instrument for flood-risk prevention. *Journal for European Environmental & Planning Law*, 14(1), 76–97. <https://doi.org/10.1163/18760104-01401005>
- Vorogushyn, S., Lindenschmidt, K. E., Kreibich, H., Apel, H., & Merz, B. (2013). Analysis of a detention basin impact on dike failure probabilities and flood risk for a channel-dike-floodplain system along the River Elbe, Germany. *Journal of Hydrology*, 436, 120–131. <https://doi.org/10.1016/j.jhydrol.2012.03.006>
- Wang, C., & Wang, J. (2022). Kilometer grid dataset of China's historical GDP spatial distribution (1990–2015) [Dataset]. *National Tibetan Plateau / Third Pole Environment Data Center*. <https://doi.org/10.12078/2017121102>
- Wang, H. (2024). Concept planning and detailed landscape design of ecological waterscape park in urban flood storage and detention area: Take Songzhuang flood storage ecological waterscape park in Tongzhou as an example. *Water Resources and Hydropower Engineering*, 55(S1), 228–232. (Chinese). <https://doi.org/10.13928/j.cnki.wrahe.2024.S1.035>
- Wang, K., Wang, Z., Liu, K., Cheng, L., Bai, Y., & Jin, G. (2021). Optimizing flood diversion siting and its control strategy of detention basins: A case study of the Yangtze River, China. *Journal of Hydrology*, 597, 126201. <https://doi.org/10.1016/j.jhydrol.2021.126201>
- Wang, K., Wang, Z., Xu, J., Mo, Y., Cheng, L., Bai, Y., et al. (2023). Floodwater utilization potential assessment of China based on improved conceptual model and multi-reservoir basin assessment method. *Journal of Hydrology*, 625, 129921. <https://doi.org/10.1016/j.jhydrol.2023.129921>
- Winemiller, K. O., McIntyre, P. B., Castello, L., Fluet-Chouinard, E., Giarrizzo, T., Nam, S., et al. (2016). Balancing hydropower and biodiversity in the Amazon, Congo, and Mekong. *Science*, 351(6269), 128–129. <https://doi.org/10.1126/science.aac7082>
- WorldPop & Center for International Earth Science Information Network (CIESIN), Columbia University. (2018). Global high resolution population denominators project [Dataset]. *WorldPop Open Population Repository (WOPR)*. <https://doi.org/10.5258/SOTON/WP00670>
- Xu, Q., Shi, Y., Bamber, J. L., Ouyang, C., & Zhu, X. X. (2024). Large-scale flood modeling and forecasting with FloodCast. *Water Research*, 264, 122162. <https://doi.org/10.1016/j.watres.2024.122162>
- Yun, S., Hudnut, K., Owen, S., Webb, F., Simons, M., Sacco, P., et al. (2015). Rapid damage mapping for the 2015Mw 7.8 Gorkha earthquake using synthetic aperture radar data from COSMO–SkyMed and ALOS-2 satellites. *Seismological Research Letters*, 86(6), 1549–1556. <https://doi.org/10.1785/0220150152>
- Zhang, Z., Giezendanner, J., Mukherjee, R., Tellman, B., Melancon, A., Purri, et al. (2025). Assessing inundation semantic segmentation models trained on high versus low resolution labels using Flood Planet, a manually labeled multi-sourced high-resolution flood dataset. *Journal of Remote Sensing*, 5, 0575. <https://doi.org/10.34133/remotesensing.0575>